

Weak Itinerant Ferromagnetism (WIFM) in MAX phase compound $\text{Cr}_{1.9}\text{Fe}_{0.1}\text{GeC}$

Suman Mondal^{1,*}, Mohamad Numan², Kurt Kummer³, Sawada Masahiro⁴, and Subham Majumdar²

¹*Department of Physics, Ben-Gurion University of the Negev, Be'er-Sheva 84105, Israel*

²*School of Physical Science, Indian Association for the Cultivation of Science (IACS),
2A & B Raja S. C. Mullick Road, Jadavpur, Kolkata 700 032, India*

³*ESRF European Synchrotron, 71 Avenue des Martyrs, F-38000 Grenoble, France and*

⁴*Hiroshima Synchrotron Radiation Center (HiSOR),
Hiroshima University-2-313 Kagamiyama, Higashi-Hiroshima 739-0046, Japan*

Magnetic MAX phase compounds are important materials for studying the two-dimensional magnetism because of their layered crystallographic structure. The hexagonal MAX phase compound Cr_2GeC is a Pauli paramagnet, and here we report the induction of an ordered magnetic state by doping Fe at the Cr site. Induced magnetism for small doping concentrations (indicated as 5% and 2.5%) is found to have a weak itinerant ferromagnetic character. The Rhodes-Wohlfarth ratio is found to be 13.29, while the coefficient of electronic heat capacity (Γ) is $27 \text{ mJ}\cdot\text{mol}^{-1}\text{K}^{-2}$ for $\text{Cr}_{1.9}\text{Fe}_{0.1}\text{GeC}$. Our x-ray magnetic circular dichroism measurement confirms that the magnetic moment arises from the Fe atom only, and Cr has negligible contribution towards the ordered moment. Our critical analysis indicates that the magnetic phase transition in $\text{Cr}_{1.9}\text{Fe}_{0.1}\text{GeC}$ follows mean field theory.

I. INTRODUCTION

Over the last few decades, there has been a growing activity in low-dimensional systems exhibiting layered sheet like structures such as graphene [1], transition metal dichalcogenides (TMDs) [2], layered van-der-Waals (vdW) materials [3] due to their potential application in the next generation beyond silicon electronics. In particular, renewed interest in thermodynamically stable exfoliable nanolaminates, known as MAX phases with a general formula $\text{M}_{n+1}\text{AX}_n$ ($n = 1, 2, 3$) has been attributed to their intriguing physical, mechanical and chemical properties. Furthermore, they also show a coexistence of both metallic and ceramic characteristics, reversible deformations, and high chemical resistance, among others [4–10]. Often MAX phases are characterized by a hexagonal layered structure, consisting of alternating layers of metal carbide or nitride (M_6X , M is an early transition metal and $\text{X} = \text{C}$ or N) integrated with an *sp*-element (A) of the periodic table [see the crystal structure depicted in Fig. 1].

Magnetic materials with layered structures are important from the fundamental as well as application point of view. The exchange coupling among the various layers is fascinating from the perspective of spintronics and magnetic memory devices. Theoretically works indicate possible spin polarization is predicted in few MAX phase material, for example Cr_2AlC , Cr_2GeC etc [11–15]. However, the first ferromagnetic (FM) MAX phase $\text{Cr}_{2-x}\text{Mn}_x\text{AlC}$ was successfully synthesized in the form of epitaxial thin films by Ingason *et al.* [16] in 2013. Subsequently, ferrimagnetic ordering was observed in the CrMnGaC thin film [17]. Furthermore, Mn-rich FM state and Mn-poor reentrant cluster glass state in polycrystalline

$\text{Cr}_{2-x}\text{Mn}_x\text{GeC}$ samples [18] were reported. Nakamura *et al.* found the spin density wave state in the nitride MAX phase Cr_2GaN and the Pauli paramagnetic state in carbide MAX phase Cr_2GaC [19]. A comprehensive study utilizing powder neutron diffraction and x-ray magnetic circular dichroism (XMCD) experiments revealed a rich magnetic phase diagram and intricate magnetic structures in the rare-earth-based MAX phase compounds $(\text{Mo}_{2/3}\text{Dy}_{1/3})_2\text{AlC}$ and $(\text{Mo}_{2/3}\text{Ho}_{1/3})_2\text{AlC}$ [20].

The carbide MAX phase compounds mostly show good metallic character with resistivity as low as few $\mu\Omega\cdot\text{cm}$ at the liquid helium temperature. The induced moment on doping magnetic elements at the M-site is found to be low [21], and they can be possible candidates for weak itinerant ferromagnet (WIFM) [22]. In a metallic magnetic system, WIFM is accompanied by low magnetic moment and generally obeys the Stoner-Wohlfarth criteria [23]. The delocalized nature of the *d* orbital in transition-metal-based intermetallic alloys and compounds plays an important role in itinerant magnetism. WIFMs show various fascinating properties such as spin fluctuations, quantum criticality, and non-Fermi liquid behavior [24–26]. Due to the delocalized nature of the moment and spin-fluctuation, the self-consistent renormalization (SCR) theory is found to be more appropriate to describe WIFMs [27]. WIFMs lie very close to the magnetic non-magnetic phase boundary, and often a small perturbation can give rise to a large change in the electronic and magnetic properties.

In the present work, we intend to induce magnetism by Fe doping in the MAX phase compound Cr_2GeC , which was previously reported to be a Pauli paramagnetic material. We doped Fe at the Cr site to prepare the solid solutions $\text{Cr}_{2-x}\text{Fe}_x\text{GeC}$ ($x = 0.05$ and 0.1), and they turned out to be WIFM, with ferromagnetic Curie points lying below the room temperature.

* mondals@post.bgu.ac.il

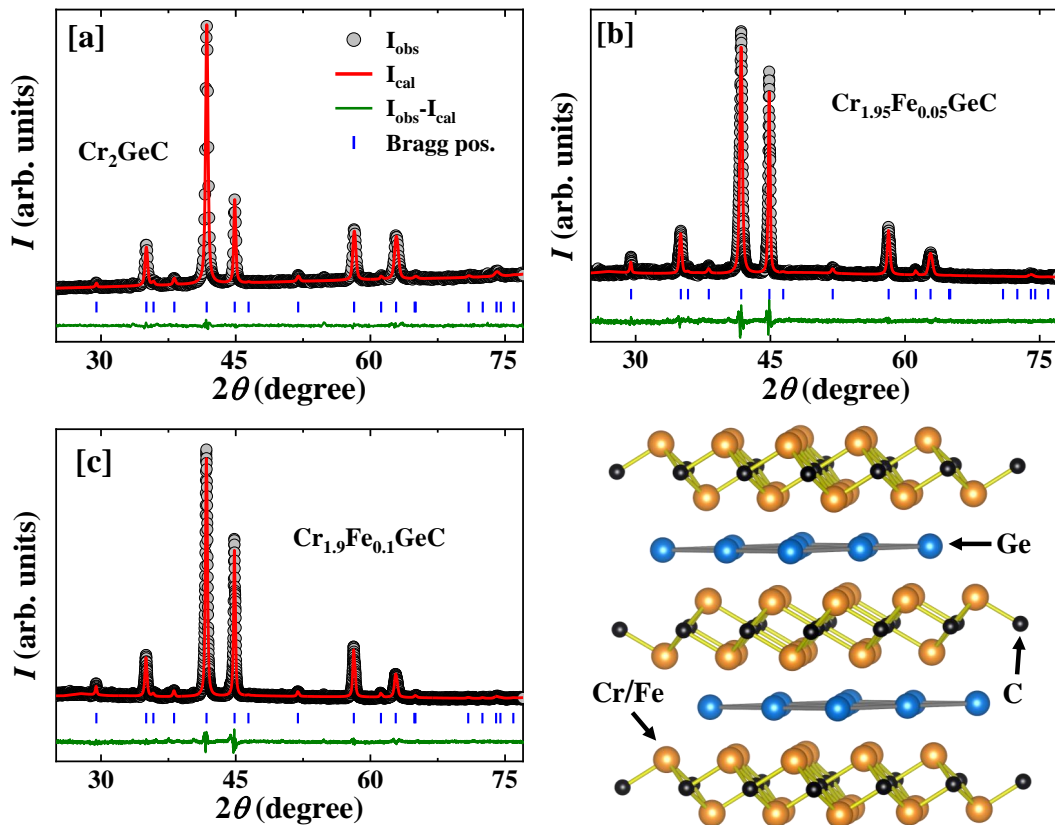


FIG. 1. (a),(b) and (c) represent the PXRD patterns recorded at room temperature for $x = 0.0, 0.05$ and 0.1 samples, respectively. The solid red lines through the data points depict the Rietveld refinement curves. (d) A perspective view of the crystal structure of Cr_2GeC -type MAX phase compound.

II. CRYSTAL STRUCTURE AND METHODOLOGY

Polycrystalline samples of $\text{Cr}_{2-x}\text{Fe}_x\text{GeC}$ ($x = 0.0, 0.05$ and 0.1) were prepared by the standard solid-state reaction route. Stoichiometric amounts of Cr, Fe, Ge and C were mixed intimately and sealed in an evacuated quartz tube (vacuum level 10^{-5} mbar). Subsequently, it was fired at 1223 K for 1 day. The powders were then pressed into pellets and heated in an evacuated quartz tube at 1273 K with several intermediate grindings. The structure and phase purity of the samples were investigated by powder x-ray diffraction (PXRD) using $\text{Cu K}\alpha$ radiation. All reflections could be indexed on the basis of the hexagonal symmetry (space group $P6_3/mcm$, no. 193) for all three samples. Rietveld refinement (solid red line: fitting curve) of the XRD data were performed using the MAUD software package [28], as depicted in Fig. 1 (a), (b) and (c). The Wyckoff positions are given in Table I. The obtained lattice parameters for Cr_2GeC are $a = 2.955 \text{ \AA}$ and $c = 12.107 \text{ \AA}$, which match well with the literature [18]. With an increase in Fe concentration, there is a small but systematic increase in both a and c .

The dc magnetization (M) of the samples was mea-

sured using a Quantum Design SQUID magnetometer (MPMS3) in the temperature (T) region of 2 to 380 K and in the magnetic field region 0 to 50 kOe. The resistivity (ρ) was measured using the four-probe technique in the temperature range of 5-300 K in a laboratory setup containing a closed-cycle helium refrigerator. The heat capacity of the $x = 0.1$ sample was measured using the relaxation technique in the Physical Property Measurement System (PPMS, Quantum Design Inc., USA), in the temperature range of 2 to 300 K.

X-ray absorption spectroscopy (XAS), as well as X-ray magnetic circular dichroism (XMCD) experiments at the Cr $L_{2,3}$ and Fe $L_{2,3}$ edges, were carried out at the D32 beamline, ESRF [29]. The experimental end station allows one to reach magnetic fields up to 90 kOe and temperature on the sample down to 5 K [30]. A bulk polycrystalline sample ($2 \times 2 \times 5 \text{ mm}^3$) was cleaved in an ultra-high vacuum chamber (base pressure of the order of 10^{-9} mbar) before being transferred to the superconducting magnet. XAS was detected in total-electron-yield (TEY) mode. XMCD spectra at the Cr $L_{2,3}$ and Fe $L_{2,3}$ edges were obtained as the difference between XAS spectra measured with opposite helicities (μ_+ and μ_-) in a finite magnetic field. XAS and XMCD measurements were also performed at the BL14 beamline of the HiSOR

TABLE I. Atomic positions (top) and lattice parameters (bottom) for $\text{Cr}_{2-x}\text{Fe}_x\text{GeC}$ with $x = 0.00, 0.05$ and 0.1 .

Sites	Wyckoff symbol	x	y	z
Cr/Fe	4 <i>f</i>	0.333	0.666	0.586
Ge	2 <i>c</i>	0.333	0.666	0.25
C	2 <i>a</i>	0	0	0

Sample	<i>a</i> (Å)	<i>c</i> (Å)
$x = 0.00$	2.954	12.107
$x = 0.05$	2.955	12.108
$x = 0.10$	2.956	12.112

synchrotron radiation center (Hiroshima, Japan).

III. RESULTS AND DISCUSSION

A. Magnetization

Fig. 2 [a] and its inset depict the T variation of M of three samples Cr_2GeC , $\text{Cr}_{1.95}\text{Fe}_{0.05}\text{GeC}$ and $\text{Cr}_{1.9}\text{Fe}_{0.1}\text{GeC}$ under $H = 100$ Oe in the field-cooled heating protocol. M is found to be small and positive for the parent sample $x = 0$ with an insignificant T -dependence, which corroborates the previous report of the Pauli paramagnetic nature of the sample [21, 31]. $x = 0.05$ and 0.1 samples order magnetically below room temperature, as evident from the rising features in the M vs T cooling data (see Fig. 2 [a]). The critical points for magnetic ordering for the $x = 0.05$ and 0.1 samples are found to be 207 K and 232 K, respectively, from the dM/dT vs. T plot (not shown here).

Fig. 2 [b] shows the M versus T data of $x = 0.1$ in the zero-field-cooled (ZFCH), field-cooling (FC) and field-cooled-heating (FCH) modes. ZFCH and FC data separate from each other at around 225 K. The FC and FCH data do not show any thermal hysteresis, indicating that the magnetic transition is second order in nature.

High-temperature magnetic susceptibility ($\chi = M/H$) have been fitted with a Curie-Weiss law (straight line fit to the χ^{-1} vs. T plot [32], depicted for $x = 0.05$ and 0.1 samples. From the Curie-Weiss fitting, the effective paramagnetic moments per formula unit (f.u.) and Curie-Weiss temperatures are found to be $\mu_{eff} = 1.85 \mu_B(\text{f.u.})^{-1}$ and $\theta_p = 272$ K, respectively for $\text{Cr}_{1.9}\text{Fe}_{0.1}\text{GeC}$ composition. For $x = 0.05$ sample, the Curie-Weiss fitting provides $\mu_{eff} = 1.54 \mu_B(\text{f.u.})^{-1}$ and $\theta_p = 225$ K. Positive θ_p indicates ferromagnetic interaction in both compositions. In particular, θ_p is higher for the highest Fe-doped sample, indicating an increase in magnetic correlation with Fe content.

Fig. 3 [a] and its inset show the isothermal M versus H data recorded at 2 K for three compounds with a maximum applied magnetic field of 50 kOe. The parent sample shows a linear variation of M with H , which is

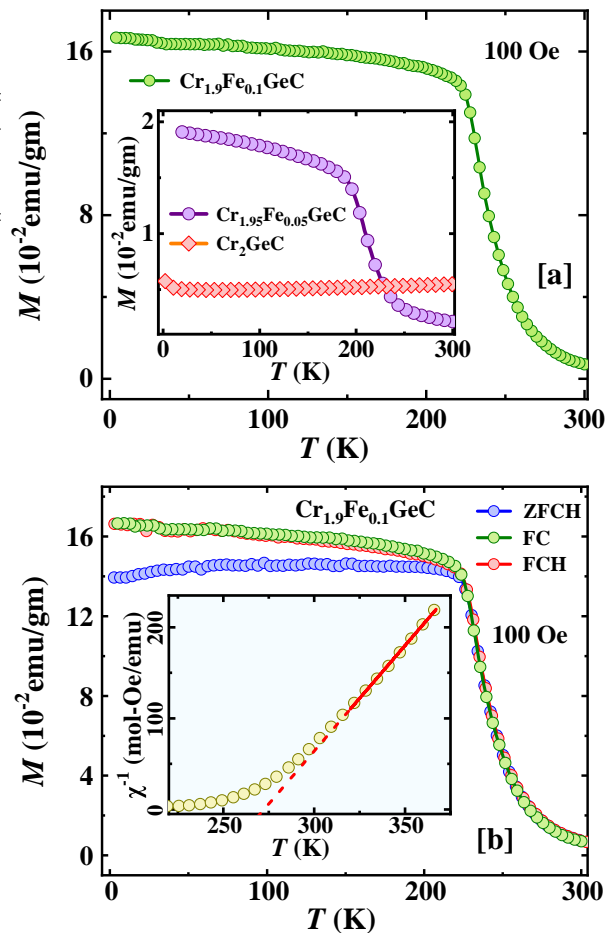


FIG. 2. (a) shows the T variation of M for $x = 0.1$ sample measured at 100 Oe during cooling. Inset compares M - T curves for $x = 0.00$ and 0.05 samples. (b) depicts M - T curves with zero field-cooled-heating (ZFCH), field cooled (FC) and field-cooled-heating (FCH) protocols, measured under $H = 100$ Oe for $x = 0.1$. The inset of (b) shows the Curie Weiss fit (solid line) to the inverse χ vs T plot at high temperature region.

expected for a Pauli paramagnet. For doped samples, the M - H curves have a typical FM nature with a sharp increase at low fields followed by a tendency toward saturation at higher fields. In particular, the isotherms for the doped samples do not completely saturate at the maximum applied field of 50 kOe. However, the value of M at 50 kOe is found to be higher for the $x = 0.1$ sample. Fig. 3 [b] shows few isotherms at different temperatures for $\text{Cr}_{1.9}\text{Fe}_{0.1}\text{GeC}$ sample. The moment observed at 2 K for 50 kOe of applied field is found to be around $\sim 0.08 \mu_B(\text{f.u.})^{-1}$ indicating the weak FM character of the sample. The coercive field of the sample is rather small, indicating a very soft FM nature. Even at 300 K, the M versus H curve is not a straight line, indicating that the sample has some short-range correlations at room temperature.

Itinerant character of a ferromagnet can be understood

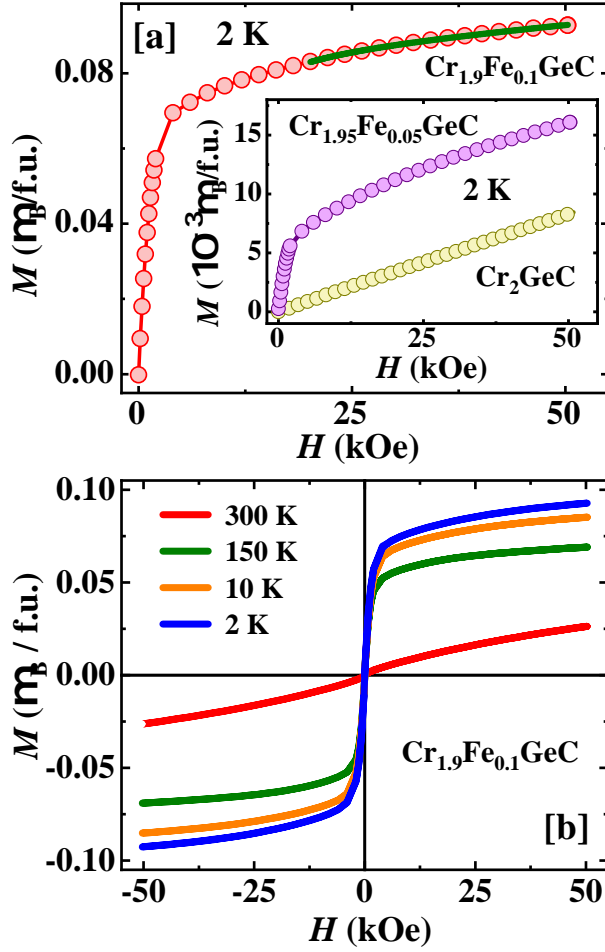


FIG. 3. (a) shows the M - H data measured at $T = 2$ K for $x = 0.1$ sample. Solid olive line represents fitting to the high field M - H data with equation $M = q_s(1 - \zeta/H^2) + \chi_H H$. Inset of (a) compares M - H curves for $x = 0.00$ and $x = 0.05$ samples. (b) depicts M - H curves measured at different temperatures for $\text{Cr}_{1.9}\text{Fe}_{0.1}\text{GeC}$.

by studying the Rhodes-Wolfarth ratio [22, 33, 34] $\text{RWR} = q_c/q_s$. The saturation moment q_s is inferred from the low-temperature M - H data, and q_c is related to the effective paramagnetic moment (obtained from the high- T Curie-Weiss fitting): $\mu_{eff}^2 = q_c(q_c + 2)$. Since $\mu_{eff} = 1.85 \mu_B(\text{f.u.})^{-1}$ for $x = 0.1$ sample, q_c turns out to be $1.103 \mu_B(\text{f.u.})^{-1}$. Fe doped Cr_2GeC does not show complete saturation, and we have used the ‘law of approach to saturation magnetization’, $M = q_s(1 - \zeta/H^2) + \chi_H H$, to fit the high-field M - H isotherm for 2 K to obtain q_s (olive solid line in Fig. 3 [a]). From fitting $q_s = 0.083 \mu_B(\text{f.u.})^{-1}$, $\zeta = 21.67 \mu_B\text{-Oe}^2(\text{f.u.})^{-1}$ and $\chi_H = 2 \times 10^{-4} \mu_B(\text{Oe-f.u.})^{-1}$. Using these values of q_c and q_s , the resulting RWR for the compound $\text{Cr}_{1.9}\text{Fe}_{0.1}\text{GeC}$ is found to be 13.29. This value of RWR is much higher than unity and is comparable to other WIFMs (see Table II) such as ZrZn_2 , Y_4Co_3 .

B. X-ray magnetic circular dichroism (XMCD)

Fig. 4 [a] and [c] show the XAS spectra for $\text{Cr}_{1.9}\text{Fe}_{0.1}\text{GeC}$ measured in TEY mode using both left (μ^+) and right (μ^-) circularly polarized x-rays at Cr $L_{2,3}$ and Fe $L_{2,3}$ edges at 5 K under an applied field of 90 kOe. The Cr $L_{2,3}$ edges XAS spectra exhibit two broad spin-orbit split peaks: the L_3 peak at 578 eV ($2p_{3/2}$) and the L_2 peak at 586 eV ($2p_{1/2}$), which result from dipole-allowed transitions from the $2p$ core to the unoccupied $3d$ states. Similarly, the Fe $L_{2,3}$ edge XAS spectra display two peaks at 707 eV ($2p_{3/2}$) and 720 eV ($2p_{1/2}$).

The XMCD signal is defined as $\Delta\mu = \mu^+ - \mu^-$, where μ^+ and μ^- denote the $L_{2,3}$ XAS spectra for photon helicity parallel and antiparallel to the magnetization direction, respectively. A strong XMCD signal is observed for the Fe element (see Fig. 4 [b]), while the Cr signal is vanishingly small (see Fig. 4 [d], almost two orders of magnitude smaller). Since XMCD provides an element-specific measurement of magnetization, it allows for the determination of the orbital ($\langle L_Z \rangle$) and effective spin ($\langle S_Z \rangle$) moments using the magneto-optical sum rules [41]. The energy-dependent variation of the XMCD data enables the calculation of these moments in terms of the following integrals:

$$\begin{aligned} \langle L_Z \rangle &= \frac{-4n_h \int_{L_3+L_2} \Delta\mu(\omega) d\omega}{3 \int_{L_3+L_2} (\mu^+ + \mu^-) d\omega} \\ &= \frac{-2qn_h}{3r} \end{aligned} \quad (1)$$

$$\begin{aligned} \langle S_Z \rangle &= \frac{n_h \left[4 \int_{L_3+L_2} \Delta\mu(\omega) d\omega - 6 \int_{L_3} \Delta\mu(\omega) d\omega \right]}{\int_{L_3+L_2} (\mu^+ + \mu^-) d\omega} \\ &= \frac{(2q - 3p)n_h}{r} \end{aligned} \quad (2)$$

Here, n_h represents the number of $3d$ holes. The quantities p , q , and r are defined as follows: $p = \int_{L_3} \Delta\mu(\omega) d\omega$ represents the integral of the XMCD signal over the L_3 edge, $q = \int_{L_3+L_2} \Delta\mu(\omega) d\omega$ is the integral on both the edges L_3 and L_2 , and $r = \frac{1}{2} \int_{L_3+L_2} (\mu^+ + \mu^-) d\omega$ denotes the integrated area of the total XAS signal over both edges after subtracting a background modeled by step functions. The integration ranges are 707–715 eV for the L_3 edge and 707–750 eV for the combined L_2 and L_3 edges. At 5 K, the calculated values of $\langle L_Z \rangle$ and $\langle S_Z \rangle$ are $0.034 \mu_B/\text{Fe}$ and $0.6 \mu_B/\text{Fe}$, respectively. The orbital moment of the Fe atom is significantly smaller than the spin moment, indicating a system with very weak spin-orbit coupling. This is expected for a $3d$ element such

TABLE II. Some basic parameters of $\text{Cr}_{1.9}\text{Fe}_{0.1}\text{GeC}$ and few other itinerant weak ferromagnets.

Sample	θ_p (K)	T_c (K)	q_c [$\mu_B(\text{f.u.})^{-1}$]	q_s [$\mu_B(\text{f.u.})^{-1}$]	RWR	Γ ($\text{mJmol}^{-1}\text{K}^{-2}$)	References
$\text{Cr}_{1.9}\text{Fe}_{0.1}\text{GeC}$	272	246	1.103	0.083	13.29	27	this work
Y_2Ni_7	40	53	0.37	0.06	6.17	52.3	[35]
ZrZn_2	33	21	0.65	0.12	5.4	45	[36, 37]
InSc_3	8	6	0.26	0.045	5.75	12	[33, 38]
Y_4Co_3	14	5	0.14	0.012	11.5	3.5	[39]
Co_3SnC	4.6	3.6	0.45	0.09	5.17	36.5	[40]

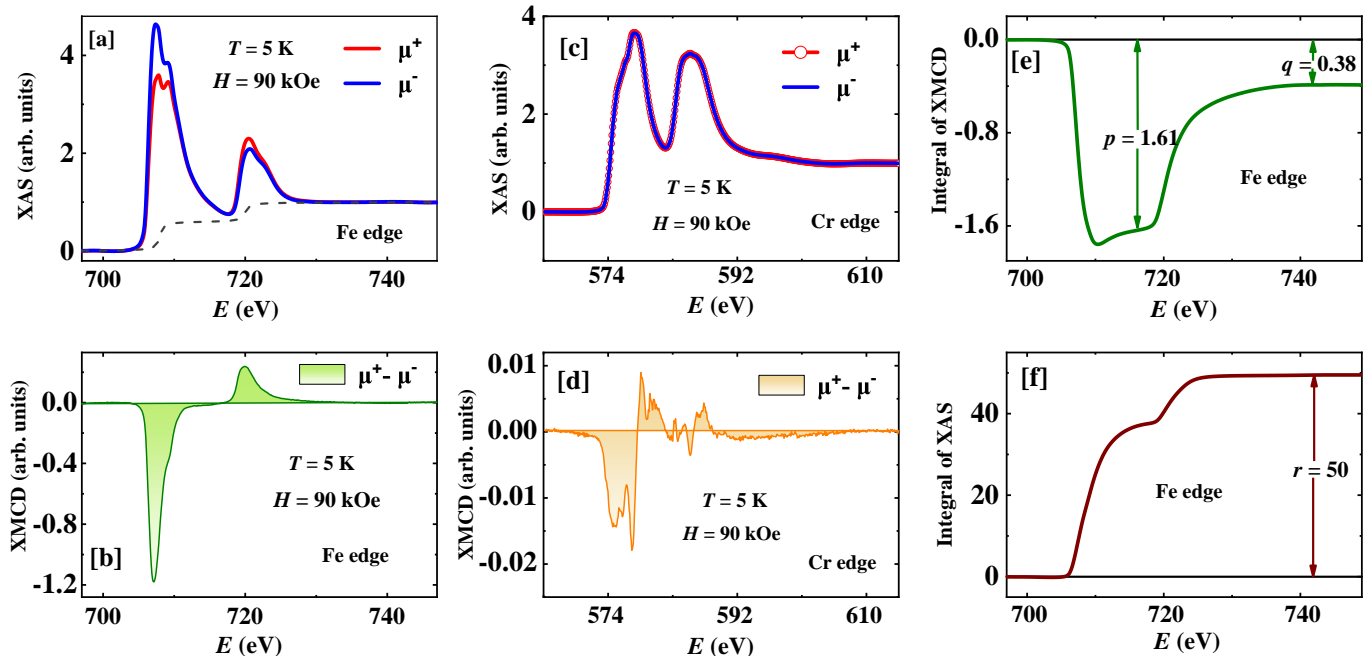


FIG. 4. (a) XAS for left circular (μ_-) polarized light, right circular (μ_+) polarized light measured in TEY mode at $T = 5$ K under $H = 90$ kOe of applied field at Fe $L_{2,3}$ for $\text{Cr}_{1.9}\text{Fe}_{0.1}\text{GeC}$ sample. Black dashed line represents the two-step background function. (b) depicts the corresponding XMCD signal from the Fe-edge. (c) and (d) respectively represent the XAS and XMCD signals from the Cr $L_{2,3}$ edges. (e) and (f) respectively show the energy variation of the integrals over the XMCD (p and q) and XAS (r) signals. p , q , and r are defined in the text.

as Fe, where the orbital moment is quenched because of strong crystal field effects. From the field-dependent bulk macroscopic magnetization measurements at 2 K, the saturation moment is approximately $0.083 \mu_B(\text{f.u.})^{-1}$ or $0.83 \mu_B/\text{Fe}$ (considering the Fe stoichiometry to be 0.1 per formula unit). This value is in close agreement with the microscopic XMCD result. We also estimated spin and orbital moments at the Cr-L edges. The reliable application of the XMCD sum rules at the Cr-L edges is usually prohibited by the too small $2p$ spin-orbit splitting causing an overlap of the Cr L_3 and L_2 edges. We can however give as upper estimates for $\langle L_Z \rangle = 0.002 \mu_B$ and, less accurately, $\langle S_Z \rangle = 0.006 \mu_B/\text{Cr}$.

Pathirage *et al.* recently studied Cr-intercalated VS_2 dichalcogenides by XMCD measurements, and a significant moment was detected at the Cr-edge [42]. XMCD studies on some layered van der Waals magnetic materials such as CrTe_2 , Fe_5GeTe_2 , and $\text{Cr}_2\text{Ge}_2\text{Te}_6$ reveal that the magnetic moment arises primarily from spin

contributions rather than orbital contributions [43–45]. Consistent with our findings, Mijit *et al.* confirmed the WIFM character of CoS_2 through XMCD measurements at the Co-L edge [46]. The spin moment at the Co site via L-edge XMCD is found to be $0.78 \mu_B/\text{Co}$, which is comparable to the Fe moment observed in our sample.

From the field variation of the element-specific XMCD signal, we can gain insight into the magnetic properties of the system [20, 47–49]. The XMCD signal from the Fe- L_3 edge was recorded as a function of the applied field, and we have plotted the area under the XMCD signal [$p(H) = \int_{L_3} \Delta\mu(\omega)d\omega$] with H in Fig. 5. The field-dependent XMCD signal mimics the macroscopic M versus H except a change in sign. In our case, the XMCD signal tends to saturate at low magnetic fields, similar to the M - H curve.

TABLE III. Spin and orbital moments obtained from XMCD measurement for some transition metal based alloys and compounds.

Sample	atom	edge	$\langle L_Z \rangle$ (μ_B/atom)	$\langle S_Z \rangle$ (μ_B/atom)	$\langle S_Z \rangle / \langle L_Z \rangle$	References
Cr _{1.9} Fe _{0.1} GeC	Cr, Fe	L	0.002, 0.034	0.006, 0.6	0.33, 17.65	this work
Cr _x VS ₂	V, Cr	L	-	0.058, 1.4	-	[42]
Cr ₂ Ge ₂ Te ₆	Cr	L	0.059	1.92	32.54	[43]
CrTe ₂	Cr	L	0.08	2.85	35.63	[44]
Fe ₅ GeTe ₂	Fe	L	0.1	1.8	18	[45]
CoS ₂	Co	L	0.049	0.782	15.96	[46]

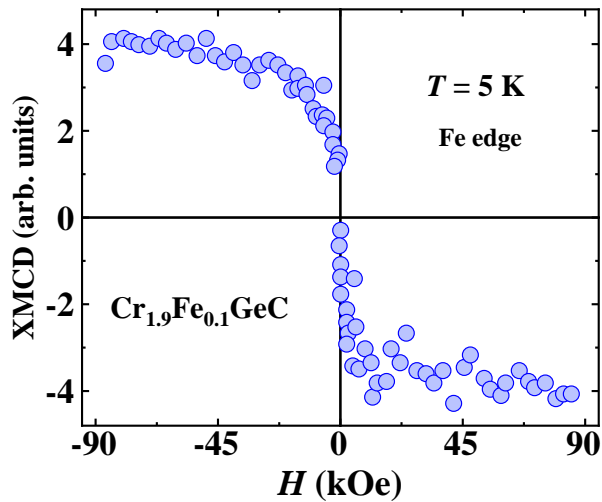


FIG. 5. Field variation of XMCD signal of the Fe- L_3 edge at 5 K for the compound Cr_{1.9}Fe_{0.1}GeC.

C. Electrical Resistivity

The zero-field ρ versus T data, shown in Figs. 6 [a] and [b], indicate a clear metallic nature for the three samples in the temperature range of 2 to 300 K. With Fe doping, ρ decreases compared to the parent sample. The residual resistivity ratio [RRR = $\rho(300\text{K})/\rho(5\text{K})$] is 45, 5 and 4.5 for Cr₂GeC, Cr_{1.95}Fe_{0.05}GeC and Cr_{1.9}Fe_{0.1}GeC, respectively. The high value of residual resistivity in the parent sample indicates that it is a high-quality sample.

$\rho(T)$ for the $x = 0.1$ sample (Fig. 6 [c]) exhibits a well defined T^2 dependence ($\rho = \rho_0 + \rho_t T^2$) at low T ($5\text{ K} < T < 20\text{ K}$), which is the usual Fermi liquid behavior in common metals resulting from electron-electron scattering. The SCR theory for WIFM predicts a term T^2 in ρ , which arises from the scattering of conduction electrons with fluctuating moments [50, 51]. In the case of Cr_{1.9}Fe_{0.1}GeC, the coefficient of the term T^2 is notably significant, measuring $5 \times 10^{-10} \Omega\text{-cm K}^{-2}$, which is approximately an order of magnitude higher than that of typical FM metals such as Ni and Fe ($\sim 10^{-11} \Omega\text{-cm K}^{-2}$). Similarly, elevated ρ_t values were observed in prototype WIFMs, such as ZrZn₂ [52] or Ni₃Al [53], and it is generally thought to be associated with spin fluctuations.

According to the SCR theory, ρ should vary with

$T^{5/3}$ just below the magnetic ordering temperature for WIFM [50]. Fig. 6 [d] shows ρ as a function of $T^{5/3}$ between 220 K and 250 K and the linear nature of the curve indicates that ρ varies as $T^{5/3}$, which is consistent with the prediction of the SCR model.

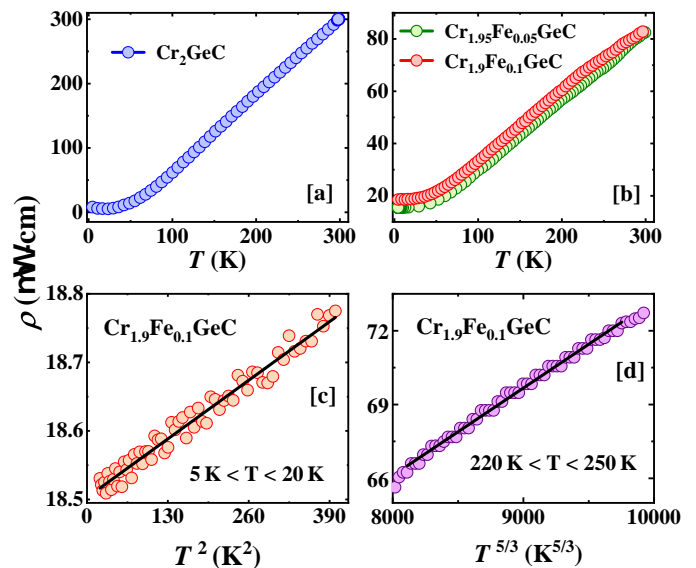


FIG. 6. (a) depicts the temperature variation of resistivity for Cr₂GeC sample, while the ρ versus T plots for $x = 0.05$ and $x = 0.1$ are shown in (b). (c) and (d) represent the ρ vs. T^2 plot ($5\text{ K} < T < 20\text{ K}$) and ρ vs. $T^{5/3}$ plot ($220\text{ K} < T < 250\text{ K}$) for $x = 0.1$ sample, respectively. The solid lines though the data points are linear fit to the curves.

D. Heat Capacity

In Fig. 7, the T variation of the specific heat (C_p) is shown in the range of 2-300 K for $x = 0.10$. No anomaly is observed around the magnetic transition. This is possibly due to the low moment and the relatively high value of the transition temperature, with the magnetic contribution being much smaller than the phonon contribution toward C_p . The low- T C_p/T vs. T^2 plot (inset of Fig. 7) shows a linear variation for $T \leq 12\text{ K}$. For $T \ll \Theta_D$ ($=$ Debye temperature), the heat capacity varies as $C/T = \Gamma + BT^2$, where Γ and B are the coef-

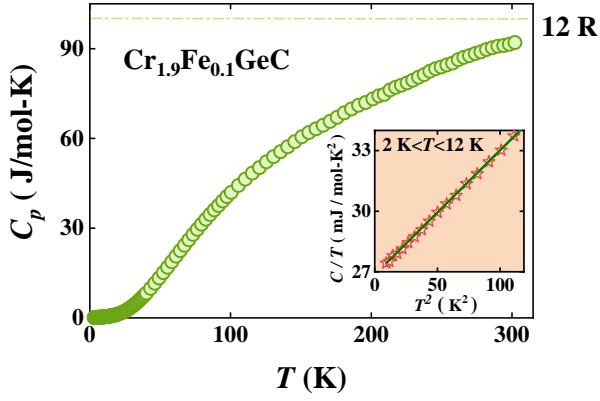


FIG. 7. Temperature variation of Specific heat for $\text{Cr}_{1.9}\text{Fe}_{0.1}\text{GeC}$ sample. Inset depicts the low temperature linear fit to the C/T vs T^2 plot.

ficients of electronic and lattice contributions of C_p , respectively. The solid line in the inset of Fig. 7 represents a fit to the data, and we obtain $\Gamma = 27 \text{ mJ mol}^{-1}\text{K}^{-2}$ and $B = 0.061 \text{ mJ mol}^{-1}\text{K}^{-4}$. The value of Θ_D obtained from B is 503 K. The value of the electronic specific heat coefficient Γ is comparable to many other WIFM systems (see Table II).

The obtained enhanced values of ρ_t and Γ from the T variation of electrical resistivity and the specific heat, respectively, indicate typical Fermi liquid-like behavior. The quantity ρ_t/Γ^2 , known as the Kadowaki-Woods ratio [54], is an important parameter to determine Fermi-liquid state in a metal. It is known that $\rho_t \propto m^{*2}$ and $\Gamma \propto m^*$, where m^* is the effective mass of conduction electrons. Therefore, within a class of materials that obey the renormalized band picture, the ratio ρ_t/Γ^2 should have a universal value. For heavy-fermion metals, the ratio is found to be close to $1.0 \times 10^{-5} \Omega\text{-cm-mol}^2 \text{K}^2\text{J}^{-2}$ [55]. However, for transition metals, the ratio has an average value of $\sim 10^{-6} \Omega\text{-cm-mol}^2 \text{K}^2\text{J}^{-2}$, which is one order of magnitude lower than that of heavy fermions. We have calculated the ratio for $\text{Cr}_{1.9}\text{Fe}_{0.1}\text{GeC}$ and it turns out to be $6.5 \times 10^{-6} \Omega\text{-cm-mol}^2 \text{K}^2\text{J}^{-2}$, which is fairly close to the value found in the case of transition metals [35, 40]. As ρ_t and Γ both increase compared to the normal metal, the Kadowaki-Woods ratio remains unchanged. This indicates that the spin fluctuations in $\text{Cr}_{1.9}\text{Fe}_{0.1}\text{GeC}$ can be well accounted for by the renormalized electronic band parameters.

E. Critical behavior

1. Arrott plot

The standard method for determining the critical exponents is the use of the Arrott plot. To construct the M^2 vs H/M Arrott plot for $\text{Cr}_{1.9}\text{Fe}_{0.1}\text{GeC}$, several isotherms were recorded around the Curie point with temperature

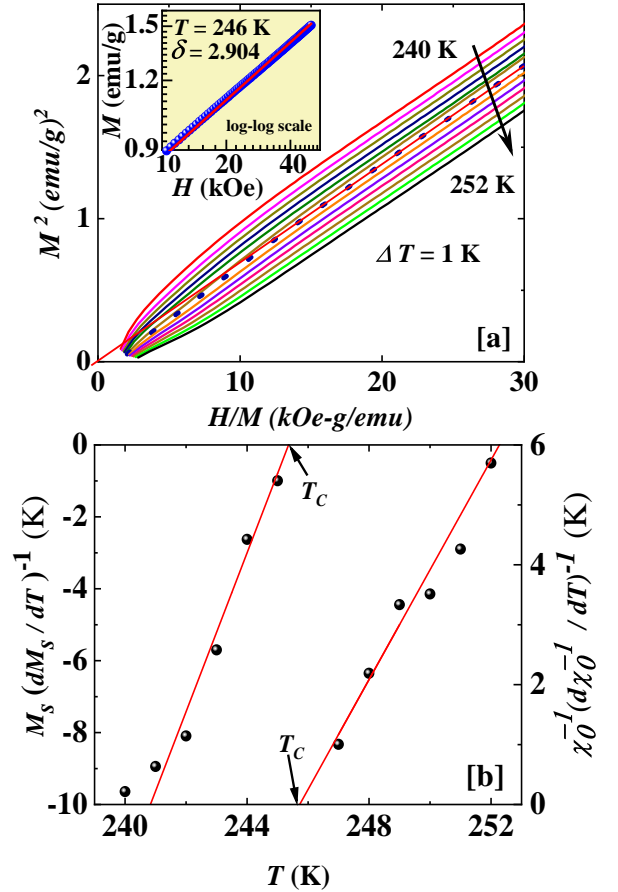


FIG. 8. (a) shows several M^2 vs (H/M) isotherms (Arrott plot) of $\text{Cr}_{1.9}\text{Fe}_{0.1}\text{GeC}$ around T_C with temperature interval $\Delta T = 1 \text{ K}$. The inset shows the M - H plot in the log-log scale at the critical temperature $T_C = 246 \text{ K}$ along with a straight line fit to the data. (b) Kouvel-Fisher plot of M_S (left axis) and χ_0^{-1} (right axis) for the sample $\text{Cr}_{1.9}\text{Fe}_{0.1}\text{GeC}$. Straight lines are the linear fit to the data.

separation $\Delta T = 1 \text{ K}$ (see Fig. 8 [a]). All the M^2 vs H/M isotherms show a positive slope indicating the magnetic transition to be second order in nature [56]. We observe that the high-field part of the Arrott curves are a set of parallel straight lines, and an extrapolation of the high-field part of the isotherm recorded at 246 K passes through the origin. It indicates that the Curie point of $\text{Cr}_{1.9}\text{Fe}_{0.1}\text{GeC}$ is $T_C = 246 \text{ K}$, which is slightly higher than the value obtained (232 K) from the curve dM/dT vs. T plot.

The high-field linear nature of the Arrott plot indicates that the system follows the mean-field theory. Near a second-order phase transition, the diverging correlation length leads to the universal scaling laws for spontaneous magnetization (M_S) below T_C , initial susceptibility ($\chi_0 = \lim_{H \rightarrow 0} M/H$) above T_C , and magnetization at T_C via a set of critical exponents β , γ , and δ , which

are defined as [57]

$$\begin{aligned} M_S(T) &= M_0|\epsilon|^\beta, \epsilon < 0 \\ \chi_0^{-1}(T) &= G(\epsilon)^\gamma, \epsilon > 0 \\ M &= XH^{1/\delta}, \epsilon = 0 \end{aligned} \quad (3)$$

Where $\epsilon = (T - T_C)/T_C$ is the reduced temperature. M_0 , G and X are the critical amplitudes.

Since, our Arrot plots are linear, we can assume the critical exponents have the mean field values, namely $\beta = 0.5$, $\gamma = 1$, and $\delta = 3$.

2. Kouvel-Fisher plot

To check the authenticity of the critical analysis, the Kouvel-Fisher (KF) method can be used. The KF plot is based on the following equations [58]:

$$\begin{aligned} \frac{M_S}{dM_S/dT} &= \frac{T - T_C}{\beta} \\ \frac{\chi_0^{-1}}{d\chi_0^{-1}/dT} &= \frac{T - T_C}{\gamma} \end{aligned} \quad (4)$$

According to the KF equation, the T -dependence of $\frac{M_S}{dM_S/dT}$ and $\frac{\chi_0^{-1}}{d\chi_0^{-1}/dT}$ should be straight lines with slopes $1/\beta$ and $1/\gamma$ respectively, and their intercept on the T -axis will result T_C . The critical exponent δ can be obtained by Widom scaling relation,

$$\delta = 1 + \gamma/\beta \quad (5)$$

We have extrapolated the high-field linear part of the M^2 versus H/M Arrot plot, and M_S^2 and χ_0^{-1} are obtained as the intercepts on the vertical and horizontal axes, respectively. Using the values of M_S^2 and χ_0^{-1} , we have constructed the KF plots as shown in Fig. 8 [b]. From the slope of the curves we obtain $\beta = 0.498$, $\gamma = 1.05$, which are quite close to the mean field values. The critical point is found to be $T_C = 245.5$ K. Using the Widom scaling relation, we obtain $\delta = 3.11$.

From eqn. 3, it is evident that the slope of the M vs. H curve in the log-log scale at T_C is equal to δ^{-1} . The slope is found to be 0.34(4) (see inset of Fig. 8 [a]) indicating $\delta = 2.904$, which is in good agreement with the value of δ obtained from the Widom scaling relation.

IV. SUMMARY AND CONCLUSION

The MAX phase compound Cr_2GeC is a Pauli paramagnet without showing any localized moment. The present investigation indicates that small Fe doping at the Cr site (2.5 %) induces ferromagnetism. The induced moment in the FM state is rather low, and the Fe-doped Cr_2GeC can be identified as a weak itinerant ferromagnetic system. The WIFM character is further evident

from the large value of Rhodes-Wolffarth ratio. We also observe a relatively large value of the electronic specific heat and the electron-electron scattering term of the resistivity, which indicate large spin-fluctuation akin to the other itinerant magnets.

Interestingly, our XMCD investigation indicates that the magnetic moment in the doped samples arises solely from Fe atoms, and Cr has almost no contribution to magnetism. The spin moment contributed by Fe is rather small, $0.6 \mu_B/\text{Fe}$, and this small value quite well corroborates the weak itinerant character of the system. A small but non-zero orbital moment indicates that the spin orbit coupling associated with Fe is weak. The XMCD signal from the Cr-L-edge is two orders of magnitude lower than that of Fe-L-edge indicating that the magnetic moment primarily arises from the Fe-site. The small moment ($= 0.006 \mu_B/\text{Cr}$ atom) observed at the Cr site could be induced by doped Fe atoms or can be induced by lattice defects.

The critical analysis around the FM Curie point of $\text{Cr}_{1.9}\text{Fe}_{0.1}\text{GeC}$ preferably assigns a mean-field model for the phase transition. This magnetic MAX phase compound has a quasi-two-dimensional layered structure. We also observed indications of spin fluctuation. Such properties do not corroborate with a mean-field model of magnetic interaction. However, the magnetic interaction in this itinerant magnet is likely to be long-range in nature arising from the indirect Ruderman-Kittel-Kasuya-Yosida (RKKY) type mechanism. In case of a long-range magnetic interaction, the spin-spin correlation length is quite high. As a result, we can assume that a single spin can interact with all other spins of the system. This in turn produces a uniform lattice field on all spins, effectively reducing the system to obey a mean-field model [61].

In a previous work, Mn doping at the Cr site of Cr_2GeC was found to induce itinerant ferromagnetism [31]. Nuclear magnetic resonance [59] and powder neutron diffraction [60] indicate that the magnetism originates primarily from the doped Mn atoms. Compared to Mn, Fe doping gives rise to a slightly higher magnetic moment along with a higher ferromagnetic T_C . For example, $\text{Cr}_{1.9}\text{Mn}_{0.1}\text{GeC}$ has a saturation moment of $0.068 \mu_B(\text{f.u.})^{-1}$ at 2 K and $T_C = 75$ K, while $\text{Cr}_{1.9}\text{Fe}_{0.1}\text{GeC}$ has $q_s = 0.083 \mu_B(\text{f.u.})^{-1}$ and $T_C = 246$ K. The present work on Fe doping and previous studies on Mn substitution indicate that C_2GeC lies close to the paramagnetic / FM boundary. Although Cr is a 3d transition metal, it does not induce any magnetic moment and long-range ordered state in Cr_2GeC . A small doping of post-Cr 3d transition metal gives rise to itinerant ferromagnetism through the Stoner mechanism because of the enhanced Coulomb repulsion among band electrons [22].

In conclusion, we have successfully induced ferromagnetism in the MAX phase compound Cr_2GeC by doping a few percent Fe at the Cr site. The resulting compositions show weak itinerant ferromagnetism and the critical exponents are found to obey the mean-field model,

presumably arising from the long-range character of the magnetic interaction. Our microscopic study categorically identifies the doped Fe as the source of the ordered magnetic moment. The FM Curie temperatures of the Fe-doped samples are close to room temperature, and they can be useful magnetic MAX-phase materials for future spintronics applications.

V. ACKNOWLEDGMENT

The authors acknowledge the European Synchrotron Radiation Facility (ESRF), France (proposal number

HC5356), and Hiroshima Synchrotron Radiation Center (HiSOR), Hiroshima University, Japan, for providing synchrotron radiation facilities.

-
- [1] W. Han, R. K. Kawakami, M. Gmitra, and J. Fabian, *Nat. Nanotechnol.* **9**, 794 (2014).
- [2] N. L. Nair, E. Maniv, C. John, S. Doyle, J. Orenstein and J. G. Analytis, *Nat. Mater.* **19**, 153 (2020).
- [3] E. C. Ahn, *npj 2D Mater. and Applications* **4**, 17 (2020).
- [4] M. W. Barsoum, *Prog. Solid State Chem.* **28**, 201 (2000)
- [5] J. Y. Wang and Y. C. Zhou, *Annu. Rev. Mater. Res.* **39**, 415 (2009).
- [6] P. Eklund, M. Beckers, U. Jansson, H. Hogberg and L. Hultman, *Thin Solid Films* **518**, 1851 (2010).
- [7] Z. Sun, H. Hashimoto, W. Tian and Y. Zou, *Int. J. Appl. Ceram. Technol.* **7**, 704 (2010).
- [8] M. Radovic and M. W. Barsoum, *Am. Ceram. Soc. Bull.* **92**, 20 (2013). Peng Tong, Xuebin Zhu, Yuping Sun, J. Alloy Compd. **680**, 452 (2016).
- [9] M. W. Barsoum, T. Zhen, S. Kalidindi, M. Radovic and A. Murugaiah, *Nat. Mater.* **2**, 107 (2003).
- [10] M. Naguib, M. Kurtoglu, V. Presser, J. Lu, J. Niu, M. Heon, L. Hultman, Y. Gogotsi and M. W. Barsoum, *Adv. Mater.* **23**, 4248 (2011).
- [11] Y. L. Du, Z. M. Sun, H. Hashimoto and M. W. Barsoum, *J. Appl. Phys.* **109**, 063707 (2011).
- [12] M. Ramzan, S. Lebegue and R. Ahuja, *Phys. Status Solidi RRL* **5**, 122 (2011).
- [13] M. Dahlquist, B. Alling and J. Rosen, *J. Appl. Phys.* **113**, 216103 (2013).
- [14] W. Zhou, L. Liu and P. Wu, *J. Appl. Phys.* **106**, 033501 (2009).
- [15] M. Mattesini and M. Magnuson, *J. Phys.: Condens. Matter* **25**, 035601 (2013).
- [16] A. S. Ingason, A. Mockute, M. Dahlqvist, F. Magnus, S. Olafsson, U. B. Arnalds and J. Rosen, *Phys. Rev. Lett.* **110**, 195502 (2013).
- [17] S. Lin, P. Tong, B. S. Wang, Y. N. Huang, W. J. Lu, D. F. Shao, B. C. Zhao, W. H. Song and Y. P. Sun, *J. Appl. Phys.* **113**, 053502 (2013).
- [18] Q. Z. Tao, C. F. Hua, S. Lin, H. B. Zhang, F. Z. Li, D. Qu, M. L. Wu, Y. P. Sun, Y. Sakkad and M. W. Barsoum, *Mater. Res. Lett.* **2**, 192 (2014).
- [19] Z. Liu, T. Waki, Y. Tabata, K. Yuge, H. Nakamura and I. Watanabe, *Phys. Rev. B.* **88**, 134401 (2013).
- [20] M. Barbier, F. Wilhelm, C. V. Colin, C. Opagiste, E. Lhotel, D. Pinek, Y. Kim, D. Braithwaite, E. Ressouche, P. Ohresser, E. Otero, A. Rogalev, and T. Ouisse, *Phys. Rev. B* **105**, 174421 (2022).
- [21] S. Lin, Y. Huang, L. Zu, X. Kan, J. Lin, W. Song, P. Tong, X. Zhu and Y. Sun, *J. Alloys and Comp.* **680** 452 (2016).
- [22] J. M. Santiago, C.L. Huang, and E. Morosan, *J. Phys. Condens. Matter* **29** 373002 (2017).
- [23] J. A. Blanco and J. Pisonero, *Eur. J. Phys.* **20**, 289 (1999).
- [24] S. S. Saxena *et al.*, *Nature* **406**, 587 (2000).
- [25] C. Pfeleiderer, S. R. Julian and G. G. Lonzarich, *Nature* **414**, 427 (2001).
- [26] M. Uhlarz, C. Pfeleiderer and S. M. Hayden, *Phys. Rev. Lett.* **93**, 256404 (2004).
- [27] T. Moriya, *J. Magn. Magn. Mater.* **14**, 1 (1979).
- [28] <http://maud.radiographema.eu>.
- [29] N.B. Brookes, and et. al., *Nuclear Instruments and Methods in Physics Research Section A: Accelerators, Spectrometers, Detectors and Associated Equipment* **903**, 175 (2018).
- [30] K. Kummer, A. Fondacaro, E. Jimenez, E. Velez-Fort, A. Amorese, M. Aspbury, F. Yakhou-Harris, P. van der Linden, and N. B. Brookes, *J. Synchrotron Radiat.* **23**, 464 (2016).
- [31] Z. Liu, T. Waki, Y. Tabata and H. Nakamura, *Phys. Rev. B* **89**, 054435 (2014).
- [32] S. Mondal, P. Yadav, A. B. Sarkar, P. Dutta, S. Giri, A. Agarwal and S. Majumdar, *J. Phys.: Condens. Matter* **34** 025801 (2022).
- [33] B. T. Matthias, A. M. Clogston, H. J. Williams, E. Corenzwit, and R. C. Sherwood, *Phys. Rev. Lett.* **7** 7 (1961).
- [34] P. Rhodes and E. Wohlfarth, *Proceedings of the Royal Society of London. Series A. Mathematical and Physical Sciences* **273**, 247 (1963).
- [35] A. Bhattacharyya, D. Jain, V. Ganesan, S. Giri and S. Majumdar, *Phys. Rev. B.* **84**, 184414 (2011).
- [36] S. J. Pickart, H. A. Alperin, G. Shirane and R. Nathans, *Phys. Rev. Lett.* **12**, 444 (1964).
- [37] E. A. Yelland, S. J. C. Yates, O. Taylor, A. Griffiths, S. M. Hayden and A. Carrington, *Phys. Rev. B.* **72**, 184436 (2005).
- [38] A. Aguayo and D. J. Singh, *Phys. Rev. B* **66**, 020401 (2002).
- [39] M. Takigawa, H. Yasuoka, Y. Yamaguchi and S. Ogawa, *J. Phys. Soc. Jpn.* **52**, 3318 (1983).

- [40] B. Wang, Y. Uwatoko, J. Cheng, and Y. Sun, *Phy. Rev. B* **102**, 085153 (2020).
- [41] C. T. Chen, Y. U. Idzerda, H.-J. Lin, N. V. Smith, G. Meigs, E. Chaban, G. H. Ho, E. Pellegrin, and F. Sette, *Phys. Rev. Lett.* **75**, 152 (1995).
- [42] V. Pathirage, S. Khatun, S. Lisenkov, K. Lasek, J. Li, S. Kolekar, M. Valvidares, P. Gargiani, Y. Xin, I. Ponomareva, and M. Batzill, *Nano Lett.* **23**, 9579 (2023).
- [43] M. Suzuki, B. Gao, G. Shibata, S. Sakamoto, Y. Nonaka, K. Ikeda, Z. Chi, Y.-X. Wan, T. Takeda, Y. Takeda, T. Koide, A. Tanaka, M. Kobayashi, S.-W. Cheong, and A. Fujimori, *Phys. Rev. Res.* **4**, 013139 (2022).
- [44] X. Zhang, Q. Lu, W. Liu, W. Niu, J. Sun, J. Cook, M. Vaninger, P. F. Miceli, D. J. Singh, S.-W. Lian, T.-R. Chang, X. He, J. Du, L. He, R. Zhang, G. Bian & Y. Xu *Nat. Commun.* **12**, 2492 (2021).
- [45] K. Yamagami, et. al., *Phy. Rev. B (L)* **103**, 060403 (2021).
- [46] E. Mijit, K. Chen, F. Choueikani, A. Di Cicco, and F. Baudelet, *Phys. Rev. B* **98**, 184423 (2018).
- [47] Sh. Yamamoto, D. I. Gorbunov, H. Akai, H. Yasumura, Y. Kotani, T. Nakamura, T. Kato, N. V. Mushnikov, *Phy. Rev. B* **101**, 174430 (2020).
- [48] Sh. Yamamoto, H. Suwa, T. Kihara, T. Nomura, Y. Kotani, T. Nakamura, Y. Skourski, S. Zherlitsyn, *Phy. Rev. B* **103**, 020408 (2021).
- [49] K. Chen, D. Lott, F. Radu, F. Choueikani, E. Otero, and P. Ohresser, *Phys. Rev. B* **91**, 024409 (2015).
- [50] K. Ueda and T. Moriya, *J. Phys. Soc. Jpn.* **75**, 605 (1975).
- [51] P. Hertel, J. Appel, and D. Fay, *Phys. Rev. B* **22**, 534 (1980).
- [52] S. Ogawa, *J. Phys. Soc. Jpn.* **40**, 1007 (1976).
- [53] S. Ogawa, *Physica B* **91**, 82 (1977).
- [54] T. Okabe, *Phys. Rev. B* **76**, 193109 (2007).
- [55] K. Kadowaki and S. B. Woods, *Solid State Commun.* **58**, 507 (1986).
- [56] B. K. Banerjee, *Phys. Lett.* **12**, 16 (1964).
- [57] H. E. Stanley, *Rev. Mod. Phys.*, **71**, 358 (1999).
- [58] J. S. Kouvel, and M. E. Fisher, *Phys. Rev.* **136**, A1626 (1964).
- [59] A. Maniv et. al. *J. Phys.: Condens. Matter* **33** 025803 (2021)
- [60] O. Rivina, E. N. Caspi, A. Pesach, H. Shaked, A. Hoser, R. Georgii, Q. Tao, J. Rosen and M. W. Barsoum, *Mat. Res. Lett.* **5**, 465 (2017)
- [61] R.T. Scalettar, *Physica A: Statistical mechanics and its application* **170**, 282 (1991).